Design of antenna-coupled lumped-element titanium nitride KIDs for long-wavelength multi-band continuum imaging

C. Ji[a], A. Beyer[b], S. Golwala[a], and J. Sayers[a]

[a]California Institute of Technology, Pasadena, CA, USA, 91125
[b]Jet Propulsion Laboratory, 4800 Oak Grove, Pasadena, CA, USA, 91109

ABSTRACT

Many applications in cosmology and astrophysics at millimeter wavelengths — CMB polarization, studies of galaxy clusters using the Sunyaev-Zeldovich effect, studies of star formation at high redshift and in our local universe and our galaxy — require large-format arrays of millimeter-wave detectors. Feedhorn, lens-coupled twin-slot antenna, and phased-array antenna architectures for receiving mm-wave light present numerous advantages for control of systematics and for simultaneous coverage of both polarizations and/or multiple spectral bands. Simultaneously, kinetic inductance detectors using high-resistivity materials like titanium nitride are an attractive sensor option for large-format arrays because they are highly multiplexable and because their high responsivity can render two-level-system noise subdominant to photon and recombination noise. However, coupling the two is a challenge because of the impedance mismatch between the microstrip exiting these architectures and the high resistivity of titanium nitride. Mitigating direct absorption in the KID is also a challenge. We present a detailed titanium nitride KID design that addresses these challenges. The KID inductor is capacitively coupled to the microstrip in such a way as to form a lossy termination without creating an impedance mismatch. A parallel-plate capacitor design mitigates direct absorption, uses hydrogenated amorphous silicon, and yields acceptable two-level-system noise. We show that an optimized design can yield expected sensitivities very close to the fundamental limit from photon and recombination noises for two relevant examples: single spectral band designs appropriate for 90 and 150 GHz for CMB polarization and a multi-spectral-band design that covers 90 GHz to 405 GHz in six bands for SZ effect studies.

Keywords: sensors, low-temperature detectors, bolometers, submillimeter-wave and millimeter-wave receivers and detectors, kinetic inductance detectors, radio telescopes and instrumentation

1. SCIENTIFIC MOTIVATION

To realize their full potential, coming missions in astrophysics and cosmology in space and on the ground require tens to hundreds of thousands of detectors in multiple mm/submm spectral bands with sensitivities approaching fundamental noise limits. These detectors must be highly multiplexable, and architectures consistent with microstrip coupling of the incoming light are strongly preferred.

If confirmed, the recent BICEP2 detection of B-mode polarization of the cosmic microwave background (CMB) due to the inflationary gravitational wave background motivates comprehensive ground- and space-based missions to map polarization over the entire sky. This is necessary not only to detect the dependence on angular scale, but also because BICEP2's B-mode measurement is limited by intrinsic statistical fluctuations of the CMB in the 2% of the sky studied to date: more sky must be mapped simply to improve the uncertainties. Independent of BICEP2, the measurement of the neutrino masses and hierarchy via an arcminute-scale ground-based CMB polarization project also requires all-sky coverage to minimize statistical uncertainties. Mapping such large areas of sky to BICEP2 depths requires massive detector counts: tens of thousands in space, as presented in the EPIC-IM study,[1] and hundreds of thousands from the ground, as discussed for a CMB Stage IV experiment.[2,3] Moreover, because the BICEP2 area is particularly low in foregrounds, these full-sky maps will require many spectral bands from 40 GHz to 300 GHz (1 mm to 7.5 mm) for foreground removal.[4]

Further author information: Send correspondence to C. Ji, cji@caltech.edu

Millimeter, Submillimeter, and Far-Infrared Detectors and Instrumentation for Astronomy VII,
edited by Wayne S. Holland, Jonas Zmuidzinas, Proc. of SPIE Vol. 9153, 915321 · © 2014
SPIE · CCC code: 0277-786X/14/$18 · doi: 10.1117/12.2056777

Imaging in multiple spectral bands in the 80-420 GHz (0.715 to 3.75 mm) range will also enable new studies of the intracluster medium (ICM) in galaxy clusters via the Sunyaev-Zeldovich (SZ) effects, specifically: the mapping of thermal and non-thermal pressure using the thermal SZ effect, the detection and study of high-temperature regions using its relativistic corrections, and the study of unvirialized bulk velocities in the ICM and the peculiar motions of entire galaxy clusters using the kinetic SZ effect. Six spectral bands are required for subtraction of radio and mm/submm galaxy foregrounds. To study individual clusters, hundreds to thousands of detectors per band may suffice, but to engage in such studies over appreciable fractions of the sky requires much larger mapping speeds and thus detector counts.

With such high detector counts, multiplexability at the $N_{mux} = 100$ to 1000 level is also a requirement. Also, as will be argued below, microstrip-coupled detectors are the approach most favored by the community, as evinced by the wide variety of development efforts focused on and deployed experiments using such detectors.

2. MOTIVATION FOR TECHNICAL APPROACH

Given the above motivations, our goal is to develop microstrip-coupled titanium nitride (TiN_x) KIDs, which promise to provide the fundamental-noise-limited performance and large detector counts needed for future mm-wave instrumentation while also being amenable to the many advantages of microstrip coupling described below. Low readout costs have already been demonstrated for TiN_x KIDs.

2.1 Advantages of Microstrip Coupling

Microstrip coupling of mm-wave optical power (hereafter "mm-wave power" or "optical power") to detectors has many advantages over direct absorption. By "microstrip coupling," we mean that optical power is received from the optical system by an element that preserves the coherence of the electromagnetic wave (an antenna or feedhorn) and is coupled to a superconducting microstripline that transmits the coherent wave to a detector. Normal metals are too lossy at mm wavelengths, while the loss in superconducting microstrip, for $h\nu < 2\Delta$ where ν is the photon frequency and Δ is the superconductor's gap energy, is generally limited only by the dielectric loss tangent of a few $\times 10^{-3}$ or better[5] (though superconductor loss is possible if contaminated[6]).

One advantage of microstrip coupling is that it enables the use of various coherent reception technologies for polarization definition and control of polarization systematics. Inherently polarization-sensitive architectures such as corrugated platelet feedhorn arrays,[7–10] phased-array antennas,[6] and lens-coupled twin-slot dipole antennas[11] have all been demonstrated with microstrip-coupled outputs. In the terminology of the EPIC studies,[1,12] the optical systematics important for creating spurious B-mode signal are differential beam size, differential pointing, differential ellipticity, differential rotation, pixel rotation, and bandpass mismatch (all between the two polarizations). Most of these polarization systematics have been studied for most of these architectures and there are either demonstrations that they satisfy the EPIC "knowledge to meet requirement" criteria or show promise for doing so.

Another advantage of microstrip coupling is that it preserves the coherent nature of the incoming light, allowing application of many traditionally "RF" structures such as hybrids, switches, and lumped-element or microstrip band-defining filters. The last is particularly useful because reception architectures can be designed to have broad bandwidths (2.5:1 and larger), so, by placing a filter bank at the microstrip output, a single pixel can be used to obtain substantial spectral information. For example, multiple broad spectral bands can be extracted from a single pixel, as in the MUSIC instrument,[13] or many narrow channels can be analyzed to perform direct detection spectroscopy, as in the SuperSpec[14–16] design.

The use of microstrip coupling also decouples the detector size from the wavelength of the incoming light. When the detector is also the optical absorber, it must be of order the wavelength in size due to diffraction. With microstrip coupling, it is the low-loss coherent mm-wave reception element that must be of order the wavelength in size, while the detector need only present a termination to the microstrip.

2.2 Sensitivity of Kinetic Inductance Detectors

Titanium nitride kinetic inductance detectors are highly multiplexable detectors capable of meeting our detector count goals while also providing fundamental-noise-limited sensitivity and low readout cost. KIDs are superconducting LC resonators. When mm-wave (or any) power breaks Cooper pairs and creates quasiparticles, the resonant frequency f_r and quality factor Q_r (which receives a contribution from quasiparticle dissipation, $Q_{i,qp}$) change and can be measured by monitoring the phase and amplitude of a probe tone at f_r. See[17] for more detail. KIDs are intrinsically multiplexable: because $Q_{i,qp} > 10^5$ at $T \ll T_c$ for attractive materials (*e.g.*, Al, TiN_x), 10^3–10^4 resonators can be probed using a single readout line and cryogenic low-noise amplifier (LNA) residing at 4 K. Moreover, KID readout costs now approach \$1/detector.

The natural measure of KID response is fractional frequency shift, $\delta f/f_r$ (which we will write as $\delta f/f$ for brevity). Assuming 1) the internal loss Q_i^{-1} contribution to Q_r^{-1} is limited by quasiparticles so $Q_i^{-1} = Q_{i,qp}^{-1}$; 2) mm-wave-generated quasiparticles dominate (total quasiparticle density $n_{qp} \gg$ thermal quasiparticle density n_{th}); 3) the resonator is optimally coupled to the readout feedline ($Q_i = Q_c$ where Q_c is the quality factor for power to escape the resonator to the feedline, so $Q_r = Q_c/2 = Q_i/2 = Q_{i,qp}/2$); and 4) pair recombination dominates over intrinsic decay in the disappearance rate of quasiparticles, the KID frequency responsivity is (*e.g.*,[17,18])

$$\frac{d(\delta f/f)}{dP_{op}} = -\frac{\beta(f_r, T_{bath})}{4\,P_{op}\,Q_i} \tag{1}$$

where $\beta(f_r, T_{bath}) > 2$ is the ratio of the imaginary and real parts of the surface impedance response from Mattis-Bardeen theory.[19] P_{op} is the mm-wave power received by the KID and is quoted at the microstrip entering the KID, after the optics and mm-wave reception elements but before considering the KID absorption efficiency.

2.2.1 KID fundamental (photon/recombination) noise

The fundamental limit to the KID noise-equivalent power for single polarization detection under the above assumptions is

$$\mathrm{NEP}^2_{fund} = \mathrm{NEP}^2_{shot} + \mathrm{NEP}^2_{Bose} + \mathrm{NEP}^2_{rec} = 2\,P_{op}\,h\nu\left[1 + \frac{P_{op}}{h\nu\,\Delta\nu} + \frac{2\,\Delta}{\eta_{abs}\,\eta_{ph}\,h\nu}\right] \tag{2}$$

where ν and $\Delta\nu$ are the mm-wave bandpass center frequency and bandwidth, η_{abs} is the efficiency for absorption of light incident on the KID from the microstrip, and $0.57 < \eta_{ph} < 1$ is the efficiency with which photons convert to quasiparticles.[20,21] The third term is recombination noise. $T_C \approx 1$ K is required for a 90 GHz band because the minimum photon energy detectable is $3.52\,k_B\,T_c/h = 2\,\Delta/h = 73$ GHz. To render thermal quasiparticles negligible, an operating temperature $T_{bath} \approx 100$ mK is required. (Lower T_c and T_{bath} are required for $\nu =$ 40 GHz, the lowest frequency desired for CMB foreground measurements.) Noise contributions from thermal quasiparticle generation/recombination and intrinsic quasiparticle decay can be neglected for our assumptions.

KID recombination noise is conceptually similar to phonon noise in TES bolometers: they are both fluctuations on power flow to the thermal bath. They are (T_c^K = KID T_c, T_c^T = TES T_c):

$$\mathrm{NEP}^2_{rec} = 2\,P_{op}\,\frac{3.52\,k_B\,T_c^K}{\eta_{abs}\,\eta_{ph}} \qquad \mathrm{NEP}^2_G = 4\,k_B\,\gamma\,(T_c^{\mathrm{T}})^2\,G_c \approx 2\,P_{op}\,\left(2\,S\,\gamma\,k_B\,T_c^{\mathrm{T}}\right)\frac{T_c^{\mathrm{T}}}{T_c^{\mathrm{T}} - T} \tag{3}$$

where $S = 2$–3 is the ratio of saturation power to mm-wave power for the TES and γ depends on the nature of the conductance to the bath. For reasonable parameters[a] at 90 GHz, we find $\mathrm{NEP}_r = 1.9\ \mathrm{NEP}_G$. This degradation has a small impact on NEP_{fund} on the ground: again, for typical 90 GHz parameters[b], one obtains $\mathrm{NEP}^K_{fund} = 31$ aW Hz$^{-1/2}$ and $\mathrm{NEP}^T_{fund} = 28$ aW Hz$^{-1/2}$. The penalty decreases as the temperatures are reduced (holding $T_c^T/(T_C^T - T)$ fixed) or as ν increases. The penalty grows at lower loading (*i.e.*, in space), but only modestly, to 25% in the limit of no Bose noise.

[a] $T = 100$ mK, $T_c^T = 200$ mK, $\gamma = 0.5$, $T_c^K = 1$ K, $\eta_{abs} = 1$, and $\eta_{ph} = 0.8$ (90 GHz). At 40 GHz, which requires T and T_c^K be reduced by a factor of 2.25, the ratio stays the same if T_c^T is reduced by the same factor and $T_c^T/(T_c^T - T) = 2$ is maintained.

[b] $\Delta\nu = 30$ GHz, optical loading of 15 K, $\eta_{opt} = 0.4$ optical efficiency to the microstrip input to the KID, single-moded reception, and a single polarization, implying $P_{op} = 2.5$ pW.

2.2.2 Readout Noise

The KID readout noise (low-noise amplifier (LNA) white noise) is

$$S_{\delta f/f}^{amp} = \frac{4\,k_B\,T_N}{Q_i^2 P_{read}} \quad \Longrightarrow \quad \mathrm{NEP}_{amp}^2 = 2\,P_{op}\,h\,\nu\,\frac{32}{[\beta(f_r, T_{bath})]^2}\,\frac{P_{op}}{P_{read}}\,\frac{k_B\,T_N}{h\,\nu} \tag{4}$$

for the same assumptions as Equation 1 and where P_{read} is the readout power on the feedline. For typical $T_N = 4$ K, $k_B\,T_N/h\,\nu = 1$ at 83 GHz, and, generally, $P_{op}/P_{read} < 1$ holds. We will see that, for TiN_x, we can render NEP_{amp} negligible for frequency response by making f_r low so β is large.[c]

2.2.3 Two-Level-System Noise

KIDs suffer two-level-system noise arising from dielectric constant fluctuations in the LC resonator's capacitor dielectric due to defect states.[22–24] Under the same assumptions as Equation 1,

$$\begin{aligned}\mathrm{NEP}_{TLS}^2 &= \frac{16\,P_{op}^2\,Q_i^2}{[\beta(f_r, T_{bath})]^2}\,S_{\delta f/f}^{\mathrm{TLS}}(f_r^0, f_a^0, T_0, V_{d,0}, E_0)\,\frac{E_0\,V_{d,0}}{\ell_C^2}\left(\frac{2\,\pi\,f_r\,C}{Q_i\,P_{read}}\right)^{1/2}\left(\frac{f_a^0}{f_a}\right)^{1/2}\left(\frac{T_0}{T_{bath}}\right)^{1.7} g\left(\frac{f_r}{f_r^0}\right)\end{aligned} \tag{5}$$

where $S_{\delta f/f}^{\mathrm{TLS}}$ is the TLS noise for a reference resonator capacitor architecture and dielectric measured at a particular resonator frequency f_r^0, audio[d] frequency f_a^0, and bath temperature T_0 for a capacitor of effective volume $V_{d,0}$ and effective electric field E_0. C and ℓ_C^2 are the capacitance and effective area of the capacitor of the resonator for which the TLS noise is being calculated. There is not a predictive theory or reliable measurement of $g(f_r/f_r^0)$, though it is expected to increase with f_r.[17] Since we will have $f_r < f_r^0$ (§3), we conservatively take g to be constant. The quantities $V_{d,0}$, E_0, and ℓ_C are most easily understood for a parallel-plate capacitor, but can be defined for other geometries. P_{op}, Q_i, and β appear via the responsivity (Equation 1). Generic statements about the level of TLS noise are not possible because $S_{\delta f/f}^{\mathrm{TLS}}$ is dependent on capacitor architecture and dielectric material, but, in our design, using an empirical value of $S_{\delta f/f}^{\mathrm{TLS}}$,[25] we render TLS noise subdominant for TiN_x by designing resonators with low f_r and thus large β (§3).

2.3 KID Multiplexability and Recent Readout Advances

The multiplexability of KIDs has been realized in multiple instruments, with enormous recent advances. NIKA[26,27] has demonstrated handling of 400 tones over a 500 MHz bandwidth.[28] MAKO[29–32] has adapted the MUSIC ROACH FPGA platform readout hardware[13,33,34] and rewritten its firmware to read out 1000 tones in the f_r range 125–250 MHz and fabricated a TiN_x KID array matching this tone density (400 tones in about 50 MHz).

KID readout systems are approaching costs of \$1/detector. The hardware cost of the room-temperature component of the now fully engineered MUSIC/MAKO readout is \$7950 per two-channel × 1000-tone module, or about \$4/tone. The cryogenic LNA cost is comparable, about \$3k per 1000-tone amplifier or \$3/tone. Thus, even at the current cost of \$7/tone, readout of 10^5 resonators is feasible at a small fraction of the cost of such an instrument (∼\$10M). A next-generation customized readout board is being developed for CCAT that will read out 4000 tones using 4 parallel readout lines (still 1000 tones/readout line) for \$2k, and multi-LNA modules will be developed to reduce LNA cost. Readout for 10^6 detectors will cost of order \$1/tone in the coming few years. Further gains may be possible, but the above satisfies the foreseeable needs.

It should be noted that the above gains have come with no increase in resonator packing density: while the resonator spacing Δf_r has shrunk by 20 from 3 MHz for MUSIC and NIKA to 150 kHz for MAKO, the fractional packing density $\Delta f_r/f_r$ remains about 10^{-3}. Rather, the required readout resources scale with $N_{mux}\,\Delta f_r = N_{mux}\,f_r\,(\Delta f_r/f_r)$, not $N_{mux}\,\Delta f_r/f_r$, so f_r is the driver.

We note that KIDs appear to offer simpler and less expensive multiplexing than TESs. While time-domain and frequency-domain multiplexing of TESs continue to advance, they do not promise N_{mux} or cost competitive with

[c] Readout noise could be made arbitrarily small if P_{read} could be made arbitrarily large, but it is limited by readout power generation of quasiparticles and kinetic inductance nonlinearity (§3).

[d] "Audio" refers to the frequency at which the mm-wave power is modulated, typically between 10^{-3} and 10^3 Hz.

KIDs. Instead, the most promising technique for TESs is RF-domain multiplexing with flux-ramp modulation, which uses KID readout techniques. It has been demonstrated with 32 TESs[35] and promises to scale to 10^3 detectors, further if combined with time-domain or frequency-domain multiplexing. However, tens of kHz of audio bandwidth ($f_r/2\,Q_r$) is required (more if combined with another multiplexing scheme). Thus, $f_r \sim 100$ MHz and $\Delta f_r/f_r \sim 10^{-3}$ ($N_{mux} \sim 10^3$) are not compatible, and so the KID readout costs do not apply: more expensive GHz readout is required.

3. DETAILED DESIGN FOR MICROSTRIP-COUPLED TiN_x KIDS

We have developed a detailed microstrip-coupled TiN_x KID design that also provides fundamental-noise-limited performance. A microstrip-coupled TiN_x KID design must address the following:

- The design must efficiently couple mm-wave power from the microstrip to the inductor of a TiN_x KID.[e]
- The design should prevent direct absorption of mm-wave power. Direct absorption is seen in current TES[10] and KID[13] geometries. Antenna-coupled designs are more susceptible than feedhorn-coupled ones, but stray light has been observed in the latter, too.[10]
- The KID two-level-system noise should be subdominant relative to NEP_{fund}.
- The available audio bandwidth, $f_r/2\,Q_r$, must be sufficient to meet the requirements of the application, which are detailed in §3.4.
- Q_r must allow $f_r \sim 100$ MHz and $\Delta f_r/f_r \sim 10^{-3}$ for the §2.3 readout costs to apply.

We discuss below how our detailed design, shown in Figure 4, addresses these considerations. We use the following fabrication layers, where "optical" and "mm-wave" refer to the reception, transmission, and absorption of mm-wave power, while "RF" and "readout" refer to the EM structure of the KID, the feedline, and the readout coupler (fabrication steps are detailed in §3.3):

- ground plane: Nb base layer (150 nm). Ground plane for the mm-wave microstrip and the coplanar waveguide (CPW) readout feedline; KID and readout capacitor bottom plate (after a cutout).
- dielectric layer(s): There are two layers of hydrogenated amorphous silicon (a-Si:H), with thicknesses 800 nm and 270 nm. They form the microstrip dielectric. The KID inductor sits entirely on top of the first layer and the KID and readout coupling capacitor use this layer for their dielectrics. The second layer provides for a capacitive mm-wave coupling between the TiN_x KID inductor and the microstrip top layer (see Figure 4). The large total thickness of a-Si:H is required to maintain a high enough microstrip impedance to match the microstrip exiting typical coherent reception elements.
- KID capacitor top layer: Nb intermediate layer (150 nm). Top plate of KID capacitor and capacitive readout coupler; CPW readout feedline center conductor.
- microstrip top layer: Nb top layer (450 nm). Signal layer of the mm-wave microstrip.
- inductor: TiN_x KID inductor layer (thickness determined in §3.4).

3.1 Design of the Millimeter-Wave Microstrip-to-KID Coupler

The cross section and plan view of the microstrip-to-KID coupler is shown in Figures 1 and 2. The coupler consists of the ground plane and top layers of the microstrip along with the TiN_x absorber film. The absorber is separated from the ground plane and the microstrip top layer by 800 nm and 270 nm of hydrogenated amorphous silicon (a-Si:H), respectively. It is meandered back and forth between the two microstrip branches.

[e]The KID responsivity scales with the square of the readout current density where the quasiparticles are created (not shown in Equation 1). The current density is highest in the inductor and can vanish in the KID capacitor.

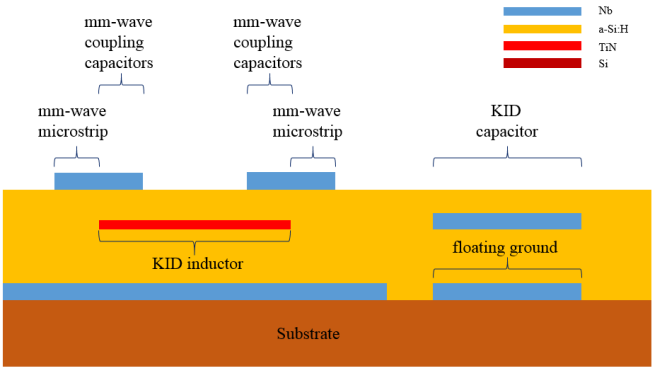

Figure 1. **Cross-sectional view.** This figure shows the cross-sectional view of the mm-wave coupler and the KID resonator. The mm-wave coupling structure is shown at left: the two branches of the post-splitter microstrip and the TiN_x absorber film. The KID capacitor is shown at right and consists of two parallel-plate capacitors in series, where the shared electrode is provided by the island in the ground plane indicated. The KID-readout feedline coupling capacitor is formed via a similar structure (these elements are not shown here). The readout feedline is a coplanar waveguide (CPW) structure that uses the ground plane layer for its ground plane and the KID capacitor top layer for its center conductor. The same metal layer used for the KID capacitor joins the KID capacitor, KID inductor, feedline coupling capacitor, and feedline center conductor together as shown in Figure 4. The planned fabrication methodology is discussed in the text.

The design begins with 4-μm-wide microstrip exiting from the coherent reception element and any bandpass-defining filters.[f] The mm-wave microstrip first splits into two 2-μm-wide microstrips that run parallel to one another with the TiN_x absorber/inductor between them. One microstrip branch undergoes a half-wavelength delay so that the mm-wave voltage on the two branches are approximately equal in magnitude but opposite in sign at any given point along their length. The capacitors formed between the microstrip top layer and the TiN_x layer apply this mm-wave voltage difference across this TiN_x layer, driving a mm-wave current and thus dissipating the incoming mm-wave power because the incoming photon energy is above the pair-breaking energy in the $T_c = 1.0\ K$ TiN_x. The capacitor geometry and dielectric thickness is chosen such that the impedance of the microstrip is negligibly modified yet the decay of power in the microstrip is dominated by loss in the TiN_x film rather than by loss in the microstrip itself (dieletric or metal loss). Furthermore, it is desirable to deposit equal power per unit length in the TiN_x film in order to obtain a uniform density of optically created quasiparticles. Thus, the coupling must be increased with position along the coupler by increasing the capacitor area with position.

The meander parameters are chosen so that the length between the two microstrips is between 0.5 and 1.5 times the mm-wave attenuation length of the microstrip formed by the TiN_x layer, the 800-nm a-Si:H layer, and the Nb ground plane to ensure that the mm-wave power that is coupled to the meander is efficiently absorbed. This attenuation length is given by

$$\lambda_{att} = 1/\alpha \qquad \text{with} \quad \alpha + i\,\beta = \gamma = \sqrt{(R + i\,\omega\,L)\,(G + i\,\omega\,C)} \approx \sqrt{i\,\omega\,R\,C} \tag{6}$$

where ω is $2\,\pi$ times the mm-wave frequency ν and R, C, L, and G are the resistance, capacitance, inductance, and dielectric conductance per unit length of this microstrip. Because the microstrip is lossy, R and C dominate over L and G.

The coupling between the microstrip branches and the TiN_x meander is varied by changing the area of the capacitor between the two layers from 3 μm^2 to 16 μm^2 according to the formula

$$\frac{1}{\lambda(L/L_0, \omega)} = \frac{1}{\lambda_0(\omega)} \frac{1}{1 - L/L_0} \tag{7}$$

[f]Narrower or wider source microstrips can be adiabatically modified in width to match to this input. The microstrip must be consistent with the above layer structure (dielectric material, film thicknesses). If this is not the case, an appropriate transformer section can be used to convert to match this microstrip's impedance. Note that this transformation can occur after any bandpass filters, so the transformer need only cover a narrow bandwidth.

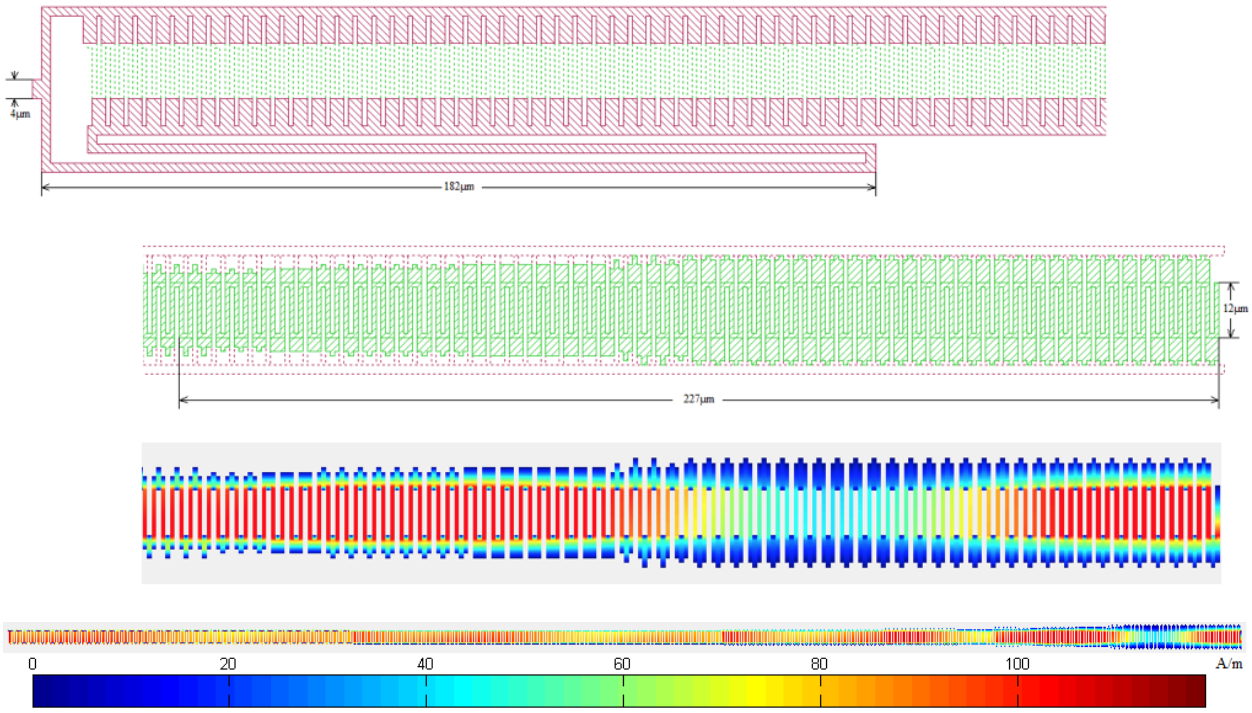

Figure 2. **Microstrip-to-KID coupler and TiN_x absorber for 150 GHz design.** The first diagram shows the input end of the coupler, including the splitter and half-wave delay line for the lower branch, with the microstrip layer opaque (red) and the TiN_x absorber layer (green) under it, while the second diagram shows the far (open) end of the coupler with the microstrip layer transparent. The third diagram shows the mm-wave current density in the same section as shown in the second diagram. The three diagrams are at the same scale. The fourth diagram shows the mm-wave current density along the entire coupler (and is zoomed out). The TiN_x absorber/inductor meanders back and forth between the two microstrip branches. The tabs extending from the microstrip top layer in the first drawing and from the TiN_x absorber/inductor in the second drawing form the electrodes of the capacitors that couple mm-wave power from the microstrip to the TiN_x absorber/inductor. The variation in the size of these coupling capacitors, done to increase the coupling with position, is visible. The third diagram shows a modest standing wave in the current density near the far end of the coupler. The full current density diagram shows steplike increases in current density at the points where the capacitor size is increased. Sonnet was used for the current density calculations.

where L_0 is the total length of the mm-wave microstrip, L is the distance from the input (left) end, $\lambda_0(\omega)$ is the attenuation length at the input end at mm-wave angular frequency ω, and $\lambda(L/L_0, \omega)$ is the attenuation length at fractional position L/L_0 and mm-wave angular frequency ω. This functional form is discretized as shown in Figure 3.

The mm-wave coupler design in principle depends on the KID inductance desired because it sets the total length of the meandered absorber. However, by varying the capacitive coupling between the microstrip and the TiN_x film, a wide range of desired length and thus inductance can be accommodated, leaving the inductance essentially a free parameter to which the coupler design conforms. A version of the microstrip-to-KID coupler optimized for the 150 GHz band has an absorption efficiency of 80% across a wide bandwidth, as shown in Figure 3, and similar performance is obtained in the other bands discussed in §3.4.

3.2 Design of the Readout Circuit

The KID layout is shown in Figure 4. The absorptive TiN_x meander acts as an inductor at low, radio-frequencies ($f \ll 2\,\Delta/h$). The two large rectangles are the top plates of two series parallel-plate capacitors formed with an island in the ground plane. A capacitive coupler to the CPW readout feedline is formed in similar fashion. All elements of the KID except for the TiN_x meander are Nb so they do not absorb mm-wave power. (In implementation, quasioptical blocking filters would be used to ensure optical power capable of breaking pairs in Nb does not reach the focal plane.)

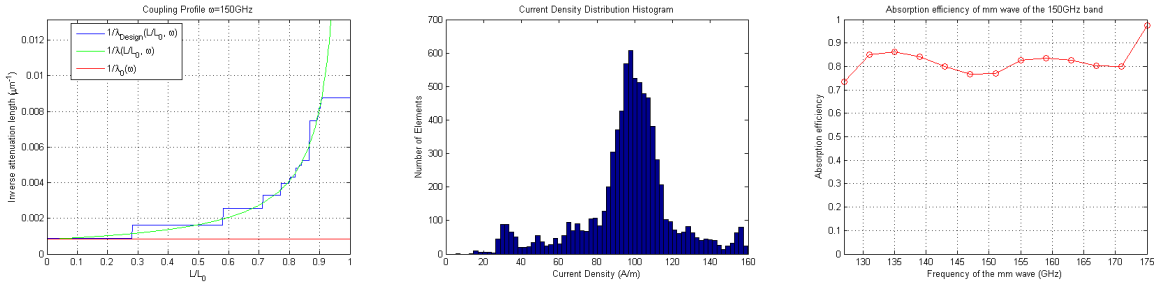

Figure 3. **Mm-wave coupling profile, histogram of current density, and mm-wave absorption efficiency.** Left: the mm-wave attenuation constant along the Nb microstrip $1/\lambda(L/L_0, \omega)$ as given in Equation 7 (not to be confused with $1/\lambda_{att}$ in Equation 6) used to obtain equal power absorption per unit length. The ideal coupling profile is shown in green and the discretized coupling profile that is implemented is shown in blue. The red line shows the value of the attenuation constant at the input end of the structure. Middle: A histogram of the mm-wave current density in the TiN_x absorber in cells of area 1 μm^2 for the 150 GHz design. The current density is very close to uniform and has a FWHM of approximately 20%. Right: Efficiency for absorption of mm-wave power incoming in microstrip. 80% absorption is obtained over the entire 150 GHz window. Sonnet was used for the calculations.

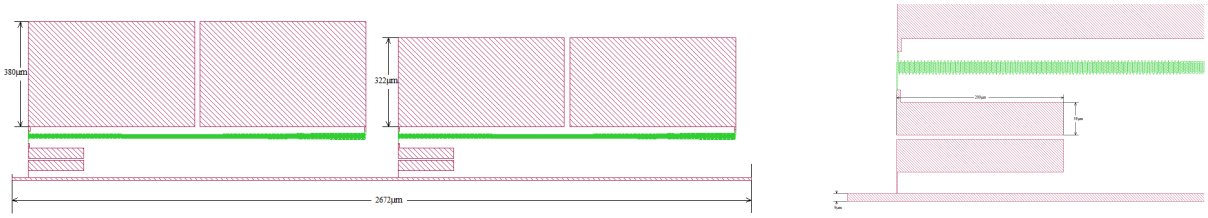

Figure 4. **KID geometry.** Left: An example of two 150GHz band resonators capacitively coupled to a single CPW readout transmission line. Right: A closeup of the readout coupling capacitor.

Because the TiN_x film has a very high normal-state resistivity (∼100 $\mu\Omega$-cm), it has a very large penetration depth λ_{pen} and corresponding large kinetic inductance $L_{k,\square} = \mu_0 \lambda_{pen}$, yielding a kinetic inductance fraction that is nearly unity, $\alpha = L_k/(L_k + L_m) > 0.98$ where L_k is the kinetic inductance and L_m the magnetic (geometric) inductance. The resulting large total inductance, $L_{tot} = L_m/(1-\alpha)$, yields a very low resonant frequency, in the 50–100 MHz range for our design, and thus a large frequency-to-dissipation response ratio $\beta(f_r, T_{bath}) \propto 2\,k\,T_{bath}/\omega_r$ for $\hbar\omega_r \ll 2\,\Delta$ where $\omega_r = 2\,\pi\,f_r$ is the readout angular frequency.

While interdigitated capacitor structures have been demonstrated to yield excellent TLS noise,[36] they have also been shown to act as antennas, receiving mm-wave light and transmitting it to the inductive portion of the KID.[13,37] This motivates the choice for the capacitor of a parallel-plate structure, which acts as a poor antenna. Direct absorption in CPW inductors has also been observed.[13,37] To prevent this, our design places the inductor above and very close to a ground plane, which enforces a short-circuit boundary condition so that the field strength of an incoming EM wave at the inductor is minimized. To our knowledge, there are no mechanisms aside from these two by which optical power can directly couple to the KID.

For ease of fabrication, the KID capacitor uses hydrogenated amorphous silicon (a-Si:H) rather than the obvious alternative, crystalline silicon. This choice brings with it the risk of two-level-system noise from the amorphous material. a-Si:H was in fact chosen because it has the lowest measured intrinsic TLS noise of any amorphous material.[25] With the dielectric fixed, the optimal capacitor area is a balance between two competing pressures. As the capacitor area A_C increases, the fractional fluctuation rms $\delta C/C$ due to TLS noise decreases as $1/\sqrt{A_C}$: the number of fluctuators grows as A_C while the fluctuation rms δC only grows as $\sqrt{A_C}$ because the fluctuators are incoherent. However, the capacitor area can appreciably reduce the focal plane area available for the coherent reception element (phased-array antennas in the case we consider here). Therefore, rather than optimizing the single-detector sensitivity NEP_{tot}, we optimize the sensitivity corrected for the loss of active area, $NEP_{tot}\,\sqrt{(A_{ant} + A_{KID})/A_{ant}}$, where A_{ant} is the antenna area and A_{KID} is the KID area. The results of the optimization will of course depend on the type and size of antenna chosen and also whether the antenna couples to detectors in a single spectral band or multiple bands.

The resonator is coupled to the readout line via a coupling capacitor C_c; see Figure 4. C_c, in series with

C_g, the capacitance between the TiN_x inductor and the Nb ground plane, determines the resonator's external coupling quality factor Q_c. In order to obtain optimal coupling to the feedline, this quality factor should be equal to Q_i, the internal quality factor, which itself should be dominated by loss due to optically created quasiparticles, $Q_{i,qp}$. These quality factors are

$$Q_c = \frac{8\,C}{C_c^2 \omega_r\, Z_0} \qquad Q_i = \frac{R}{\omega_r L_{tot}} \tag{8}$$

$\omega_r = 2\,\pi\,f_r$ is the resonant angular frequency of the KID, Z_0 is the impedance of the CPW readout line, chosen to be 50 Ω for convenience. R is the resistance of the inductor, which should be dominated by optically generated quasiparticles and receive negligible contribution from thermal quasiparticles or other loss mechanisms (e.g., metal loss), and L_{tot} is the total inductance. The coupling capacitance is designed to satisfy the $Q_c = Q_{i,qp}$ criterion.

For a given detector design, the KID resonant frequency is varied in a straightforward fashion by varying the KID capacitor area. Figure 4 shows two 150 GHz KIDs designed for different resonant frequencies in this manner.

3.3 Detector Fabrication

We anticipate fabricating the structure on high-resistivity silicon substrates as follows:

1. A 150-nm thick layer of Nb will be deposited by DC-magnetron sputtering and patterned by plasma etching for the ground plane. The patterning will define the KID and readout coupling capacitor bottom electrode islands. It will also define the edges of the ground plane of the CPW readout feedline. This layer also serves as the ground plane for phased-array antenna applications, and so slots will be cut in the ground plane for the antenna slot dipoles. A border around three edges of the device will also be removed to allow a gold heat-sinking layer that makes direct contact to the silicon substrate later.

2. A 800-nm thick layer of a-Si:H will be deposited by chemical vapor deposition. No patterning is necessary except to expose a border around three edges of the device for the gold heat-sink layer and at the fourth edge to allow direct electrical contact to the ground plane via wirebonds to the device holder.

3. A 20-nm thick layer of TiN_x will be deposited and patterned by plasma etching for the KID inductor.

4. The 150-nm thick layer of Nb for the KID and readout coupling capacitor top electrodes and the CPW feedline center conductor will then be deposited and patterned. It must make direct contact to the TiN_x to form the KID. It would be simplest to use liftoff for this step, but there are concerns that the Nb will become contaminated by photoresist: during either the ion mill step that necessary to remove any oxide on the TiN_x so the TiN_x-Nb contact is fully conducting, or during the deposition of the Nb. Such contamination is known to be possible, affecting the microstrip properties.[6] An alternate process would be to deposit SiO_2 and pattern it by plasma etching to create a stencil identical to the liftoff stencil. Ion milling and Nb deposition can then proceed as before. The Nb would be patterned using plasma etching, and then the SiO_2 removed by plasma etching.

5. A 270-nm thick layer of a-Si:H will be deposited by chemical vapor deposition to complete the microstrip dielectric. Again, a border must be removed around the edge of the device.

6. A 450-nm thick layer of Nb will be deposited by DC-magnetron sputtering and patterned by plasma etching to define the microstrip top layer of the microstrip-to-KID mm-wave coupler and for the phased-array antenna. Again, a border around three edges of the device must be removed, and also the fourth edge must be patterned to preserve the CPW feedline gap.

7. A 350-nm thick layer of Au will be deposited by DC-magnetron and patterned using liftoff process. This film provides a 1-mm border around three edges of the device that is used to heat sink the device using Au wirebonds to the device holder. The Au film overlaps the Nb ground plane so that the wirebonds act to provide RF continuity between the ground plane and the device holder.

3.4 Parameters and Results of Optimization

We optimize the above design for two distinctly different implementations to demonstrate that fundamental-noise-limited sensitivity is achievable with this design under a wide range of conditions. In addition to optimizing for sensitivity, we also require that the audio bandwidth available, which is given by $f_r/2\,Q_r$, is consistent with the desired signal bandwidth for the application. This requirement couples f_r and $Q_i = Q_{i,qp}$. The two applications and the assumptions made are discussed below and given in detail in Table 1:

- **CMB polarization science band mapping**
  It is widely recognized that 90 and 150 GHz are critical bands for CMB polarization studies because they are near the frequency at which the expected intensity of polarized foreground emission from our galaxy (dust and sychrotron) is minimized. For small patches of sky (a few % up to 10%), this minimum is expected to be near 150 GHz, while it shifts down to as low as 70 GHz when the whole sky is considered.[4] Thus, they present excellent test cases for optimization. We consider detectors coupled to monochromatic, polarization-sensitive, superconducting phased-array antennas, such as those used for the BICEP2, Keck Array, SPIDER, and BICEP3 experiments.[6] In both bands, it is assumed the antenna is 6.66 mm on a side. Each antenna couples to two detectors, one for each polarization, so the detectors are optimized assuming single-polarization optical loading. We assume the same optical loadings in Rayleigh-Jeans temperature units as the EPIC-IM study,[1] and we assume optical efficiencies typical for these antenna designs combined with the necessary quasioptical filtering of thermal infrared and out-of-band radiation. An audio bandwidth requirement of 500 Hz is assumed, which meets the requirements of EPIC-IM. The noise is evaluated at 1 Hz, corresponding to an angular multipole of roughly $\ell = 100$ for EPIC-IM, matching the peak of the inflationary B-mode power spectrum. Note that the 90 and 150 GHz designs are separately optimized.

- **Sunyaev-Zeldovich effect science**
  As discussed in Section 1, the next generation of SZ effect studies of galaxy clusters will require six spectral bands from 90 GHz to 420 GHz. For this application, we are in parallel developing multi-scale phased array antennas, which use a single antenna structure to cover this wide frequency range in a single detector pixel. The pixel size is varied in a binary fashion with frequency so that all spectral bands use pixels that approximately match the corresponding frequency-dependent Airy function spot size at the focal plane. For the optimization, the key consideration is that A_{KID} must incorporate the area of all the KIDs for the six bands, including the fact that, at higher frequencies, a single antenna structure may couple to multiple detectors in a single band. It is assumed that the antenna structure is 6.66 mm on a side and that this corresponds to a single pixel at 90 and 150 GHz, 4 pixels at 220 and 290 GHz, and 16 pixels at 350 and 420 GHz. We assume optical loadings appropriate for the planned CCAT 25-m submm/mm telescope on Cerro Chajnantor, including the emission from the telescope itself (assumed to have 5% emissivity for $\nu < 300$ GHz and 10% emissivity for $\nu > 300$ GHz) and the atmosphere for precipitable water vapor = 0.55 mm (corresponding to 42% in the cumulative distribution function). The optical loading from the instrument itself is assumed to be such that the total loading is increased by an *ad hoc* factor of $\sqrt{3}$ from telescope and sky loading alone. The audio bandwidth requirement is based on assuming a scan speed of 2° deg/sec and beam FWHM appropriate to the 25-m aperture diameter and scaling with wavelength. The audio frequency at which the TLS noise is evaluated is 10 Hz because it corresponds to $12'$ for $v_{tel} = 2^\circ$/sec, a reasonable scale at which one would like full image fidelity for cluster studies.

In both cases, $T_c = 1.0$ K and $T_{bath} = 0.1$ K are assumed. This T_c is the highest value consistent with 90 GHz operation ($2\,\Delta/h = 73$ GHz), and T_{bath} has been chosen to reduce the thermal quasiparticle population to negligible levels. η_{ph} is the efficiency for conversion of photon energy into quasiparticles, which is known to asymptote to 0.57 for $h\,\nu \gg 2\,\Delta$[20] and must asymptote to unity at $h\,\nu = 2\,\Delta$. We assume linear behavior in the range $h\,\nu = 2\,\Delta$ to $h\,\nu = 2\,\Delta/0.57$. For TiN_x materials parameters, we assume a recombination constant $R = 100\ \mu\text{m}^3\ \text{s}^{-1}$, an intrinsic lifetime $\tau_0 = 100\ \mu$s (as measured in[38]), and a single-spin density-of-states $N_0 = 3.5 \times 10^{10}\ \mu\text{m}^{-3}\ \text{eV}^{-1}$.[31] The amplifier noise assumed is $T_N = 4$ K as discussed in connection to Equation 4. We require that the design achieve a multiplex factor of N_{mux}, which factors into the constraint on Q_i and f_r. P_{read} is the assumed readout power, chosen to be a reasonable level based on experience. A larger

Band-Independent External Parameters

Quantity	1-band CMB pol	6-band SZ
T_c	1.0 K	
2Δ	300 μeV	
$2\Delta/h$	73 GHz	
A_{tel}	N/A	491 m^2
v_{tel}	2.45° s^{-1}	2° s^{-1}
N_0	3.5×10^{10} μm^{-3} eV^{-1}	
R	100 μm^3 s^{-1}	
τ_0	100 μs	
T_{bath}	0.1 K	
T_N	4.0 K	
N_{mux}	1000	
P_{read}	10.0 pW	1.0 pW
J^*	6.0 mA μm^{-2}	
f_a	1 Hz	10 Hz

Band-Dependent External Parameters

Quantity	1-band CMB pol		6-band SZ					
ν [GHz]	90	150	90	150	225	285	350	400
$\Delta\nu$ [GHz]	35	47	35	47	45	50	34	30
T_{sky} [K]			5	6	10	14	30	57
T_{tel} [K]			13	13	13	13	27	27
T_{instr} [K]			14	14	17	20	41	61
T_L [K]	1.35	0.79	32	33	40	47	98	145
FWHM$_{beam}$ [′]	8.4	5.6	0.53	0.37	0.22	0.20	0.14	0.12
ℓ_{ant} [mm]	6.66	6.66	6.66	6.66	3.33	3.33	1.66	1.66
A_{ant} [mm^2]	44.4	44.4	44.4	44.4	11.1	11.1	2.8	2.8
η_{op}	0.42	0.64	0.26	0.40	0.34	0.38	0.26	0.29
P_{op}	0.27	0.33	4.0	8.6	8.4	9.9	12.0	17.4
η_{ph}	0.81	0.57	0.81	0.57	0.57	0.57	0.57	0.57

Table 1. **Parameters specified externally for the optimization.** Definitions: T_c = superconductor transition temperature; Δ = superconductor gap energy; A_{tel} = telescope area for 6-band SZ (not relevant for CMB polarization); v_{tel} = telescope scan speed; N_0 = single-spin density of states, R = recombination constant; τ_0 = intrinsic quasiparticle decay lifetime; T_{bath} = operating temperature; T_N = amplifier noise temperature; N_{mux} = required multiplex factor; P_{read} = readout power for KID; J^* = superconducting critical current density; f_a = characteristic audio frequency of signal (at which TLS noise is evaluated); ν = spectral band center; $\Delta\nu$ = spectral bandwidth; T_{sky}, T_{tel}, T_{instr}, T_L = Rayleigh-Jeans optical loading from atmosphere, telescope, instrument, and total; FWHM$_{beam}$ = beam FWHM; ℓ_{ant}, A_{ant} = side length and area of phased-array antenna; η_{op} = optical efficiency (does not include efficiency loss due to single polarization); P_{op} = optical loading power received at detector (prior to conversion to quasiparticles, after all optical efficiencies and polarization selection); η_{ph} = efficiency for conversion of photon energy to quasiparticles.

readout power is assumed for the CMB polarization application because of the more demanding sensitivity required. J^* is the critical current density, $J^* = \sqrt{\pi\, N_0\Delta^3/\hbar\rho_n}$ in BCS theory. $J < J^*$ is required to avoid nonlinear kinetic inductance effects such as bifurcation of the resonance.[39] We recall that, for TLS noise, we start from the value of $S^{\rm TLS}_{\delta f/f}$ in[25] and scale it according to Equation 5. In particular, we evaluate it at the f_a given in the table deemed relevant for the particular science as discussed above.

There is not space here to describe in detail all the pressures on the optimization and how the sensitivity scales with various parameters. Rather, we only present the results of the optimization in Table 2 and make the following comments:

- The film thickness and width saturate at the minimum values allowed, 20 nm and 1 μm. This limits have been chosen ensure robust fabrication.

Optimized Parameters

Quantity	1-band CMB pol		6-band SZ					
ν [GHz]	90	150	90	150	225	285	350	400
Varied Parameters								
t	20 nm		20 nm					
t_d	800 nm		800 nm					
ℓ_L [mm]	13.0	7.9	6.5	7.9	5.3	8.2	6.7	5.9
w [μm]	1.1	1.0	1.03	1.00	1.01	1.00	1.01	1.02
ℓ_C [mm]	0.65	0.75	0.91	0.71	0.73	0.51	0.52	0.59
Derived Geometrical Parameters								
A_L [mm^2]	0.014	0.008	0.007	0.008	0.005	0.008	0.007	0.006
V [μm^3]	279	163	134	158	107	165	136	121
A_C [mm^2]	0.42	0.56	0.83	0.51	0.53	0.26	0.27	0.34
$A_{ant}/(A_{ant}+A_{KID})$	0.99	0.99	0.75					
Derived RF Parameters								
λ_{pen}	30 μm		30 μm					
L [μH]	0.47	0.30	0.44	0.55	0.37	0.57	0.46	0.40
C [pF]	14	19	27	17	18	9	9	11
f_r [MHz]	62	68	46	52	63	71	78	74
$Q_{i,qp}$ [10^4]	18	14	3.9	3.1	2.2	2.3	1.8	1.4
J [mA μm^{-2}]	4.7	5.1	0.8	0.7	0.6	0.5	0.4	0.4
E [kV/m]	7.2	5.3	2.8	3.0	2.2	3.1	2.5	2.1
$S^{TLS}_{\delta f/f}$ [10^{-19} Hz^{-1}]	6.4	6.7	8.6	13.1	16.6	24.7	29.0	27.8
Derived Quasiparticle Parameters								
n_{qp} [μm^{-3}]	450	550	2700	3050	3700	3200	3900	5000
τ_{dyn} [μs]	10.0	8.3	1.8	1.6	1.3	1.5	1.3	1.0
Derived Responsivity								
η_{abs}	0.83	0.83	0.83	0.83	0.84	0.83	0.83	0.83
$\delta f/f$ Responsivity [10^6 W^{-1}]	170	170	64	34	42	31	31	27
Derived Sensitivity								
NEP$_{ph}$ [aW Hz$^{-1/2}$]	6.1	8.4	37	69	76	92	118	172
NEP$_{rec}$ [aW Hz$^{-1/2}$]	6.0	7.9	25	43	43	47	51	62
NEP$_{amp}$ [aW Hz$^{-1/2}$]	0.5	0.6	6	14	16	21	27	38
NEP$_{TLS}$ [aW Hz$^{-1/2}$]	4.7	4.8	14	34	31	51	55	61
NEP$_{fund}$ [aW Hz$^{-1/2}$]	8.7	11.7	45	82	87	103	129	183
NEP$_{tot}$ [aW Hz$^{-1/2}$]	9.9	12.7	47	89	93	115	140	193
Area-corrected NEP$_{tot}$/NEP$_{fund}$	1.14	1.08	1.21	1.25	1.23	1.29	1.26	1.22
NEFD [mJy sec$^{1/2}$]	N/A		1.8	2.2	2.4	2.6	5.6	8.1
NET$_{\rm RJ}$ [μK$_{\rm RJ}$ sec$^{1/2}$]	35	22	270	240	310	310	800	1100
NET$_{\rm CMB}$ [μK$_{\rm CMB}$ sec$^{1/2}$]	43	37	330	420	1000	1800	10000	26000

Table 2. **Results of optimization.** Parameter definitions: t = TiN$_x$ film thickness; t_d = KID capacitor dielectric film thickness; ℓ_L = inductor length; w = inductor width; ℓ_C = KID capacitor side length; A_L = inductor area; V = inductor volume; A_C = capacitor area; $A_{ant}/(A_{ant}+A_{KID})$ = fraction of focal plane area used for antennas (active fraction); λ_{pen} = superconductor penetration depth; L = KID inductance; C = KID capacitance; f_r = KID resonant frequency; $Q_{i,qp}$ = KID internal (optically generated quasiparticle) loss quality factor; J = KID current density (should be below J^*); E = electric field in KID capacitor; $S^{TLS}_{\delta f/f}$ = TLS noise at f_a and for the given device parameters and readout conditions; n_{qp} = quasiparticle density (all optically generated; thermal quasiparticle density is negligible); τ_{dyn} = quasiparticle lifetime under optical load; η_{abs} = microstrip-to-KID coupler efficiency; $\delta f/f$ Responsivity = $d(\delta f/f)/dP_{op}$ as given in Equation 1. The NEPs are given in the order: photon (shot + Bose); recombination; amplifier; and TLS noise. NEP$_{fund}$ is the sum of photon and recombination noise: it is the fundamental noise limit given the assumed optical loading and T_c. The NEP$_{tot}$/NEP$_{fund}$ ratio indicates how far the design is from the fundamental limit, and the area correction accounts for the fraction of the focal plane lost to the KID capacitors by degrading the ratio by $\sqrt{(A_{ant}+A_{KID})/A_{ant}}$. The NEPs are converted to NEFD, NET$_{\rm RJ}$, and NET$_{\rm CMB}$ assuming the given A_{tel}, $\Delta\nu$, η_{op}, and band centers.

- An explicit optimization over dielectric thickness was not performed but rather the maximum value possible to robustly fabricate was assumed. At fixed capacitor area, increasing the thickness reduces the TLS noise (in $\delta C/C$ or $\delta f/f$ units) as noted above in the discussion of the optimization pressures on A_C, so choosing the maximum value is sensible.
- The resonant frequencies tend to saturate at the lower bound allowed by the audio bandwidth and the multiplex factor because of the $1/f_r$ dependence of the responsivity.
- For the six-band SZ design, the quality factors Q_i are somewhat low, on the order of 10^4, because the high scanning speed of the telescope combined with the small beams yields the most demanding audio bandwidth requirements. One could satisfy this requirement either by increasing f_r or reducing Q_i, but we find reducing f_r is preferred.
- The current densities are below the critical current density as desired, though they are quite close for the CMB polarization design.
- A deficiency of this optimization is that readout generation of quasiparticles has not been considered. This should not play much of a role for the 6-band SZ design because $P_{read} \ll P_{op}$, but it could be important for the CMB polarization design in which $P_{read} \gg P_{op}$.
- In all cases, the optimization is able to yield total sensitivities within 10–25% of the fundamental noise limit, as was our goal.

If the demonstrated TLS noise level of a-Si:H cannot be obtained, the KID and readout coupling capacitors can be made using crystalline silicon using SOI wafers, but the fabrication would substantially more complicated.

4. CONCLUSION

We have presented a design for a microstrip-coupled titanium nitride KID. We have optimized the design for two applications, space-based CMB polarization and ground-band SZ effect, and shown that it is capable of providing sensitivities within 10–25% the fundamental noise limits for these configurations. We are currently in the midst of fabricating devices for the six-band SZ effect design, which we will use to test the design and refine the optimizations presented here.

ACKNOWLEDGMENTS

This work has been supported by the California Institute of Technology, the Norris Foundation, the JPL Research and Technology Development Fund, and the NASA SAT program. We thank the following colleagues for useful discussions and advice: M. Kenyon, R. LeDuc, C. McKenney, E. Shirokoff, and J. Zmuidzinas.

REFERENCES

[1] J. Bock *et al.*, "Study of the Experimental Probe of Inflationary Cosmology (EPIC)-Intemediate Mission for NASA's Einstein Inflation Probe." astro-ph.co/0906.1188 (2009).

[2] K. N. Abazajian *et al.*, "Inflation Physics from the Cosmic Microwave Background and Large Scale Structure." astro-ph.CO/1309.5381 (2013). Report from the *Dark Energy and CMB* working group for APS DPF CSS2013.

[3] K. N. Abazajian *et al.*, "Neutrino Physics from the Cosmic Microwave Background and Large Scale Structure." astro-ph.CO/1309.5383 (2013). Report from the *Dark Energy and CMB* working group for APS DPF CSS2013.

[4] J. Dunkley *et al.*, "Prospects for polarized foreground removal," in *CMB POLARIZATION WORKSHOP: THEORY AND FOREGROUNDS: CMBPol Mission Concept Study*, S. Dodelson, D. Baumann, A. Cooray, J. Dunkley, A. Fraisse, M. G. Jackson, A. Kogut, L. Krauss, M. Zaldarriaga, and K. Smith, ed., *American Institute of Physics Conference Series* **1141**, 222–264, American Institute of Physics, Melville, NY (2009). astro-ph/0811.3915.

[5] J. M. Martinis *et al.*, "Decoherence in Josephson Qubits from Dielectric Loss," *Phys. Rev. Lett.* **95**, 210503/1–4 (Nov. 2005).

[6] R. O'Brient *et al.*, "Antenna-coupled TES bolometers for the Keck array, Spider, and Polar-1," in *Society of Photo-Optical Instrumentation Engineers (SPIE) Conference Series*, **8452**, 84521G/1–11, SPIE, Bellingham, Washington (2012). astro-ph.IM/1208.1247.

[7] M. D. Niemack *et al.*, "ACTPol: a polarization-sensitive receiver for the Atacama Cosmology Telescope," in *Society of Photo-Optical Instrumentation Engineers (SPIE) Conference Series*, **7741**, SPIE, Bellingham, WA (2010).

[8] J. Hubmayr *et al.*, "An All Silicon Feedhorn-Coupled Focal Plane for Cosmic Microwave Background Polarimetry," *J. Low. Temp. Phys.* **167**, 904–910 (2012).

[9] J. McMahon *et al.*, "Multi-chroic Feed-Horn Coupled TES Polarimeters," *J. Low. Temp. Phys.* **167**, 879–884 (2012).

[10] J. W. Henning *et al.*, "Feedhorn-coupled TES polarimeter camera modules at 150 GHz for CMB polarization measurements with SPTpol," in *Society of Photo-Optical Instrumentation Engineers (SPIE) Conference Series*, **8452**, 84523A/1–15, SPIE, Bellingham, Washington (2012).

[11] K. Arnold *et al.*, "The bolometric focal plane array of the POLARBEAR CMB experiment," in *Society of Photo-Optical Instrumentation Engineers (SPIE) Conference Series*, **8452**, 84521D/1–12, SPIE, Bellingham, Washington (2012).

[12] J. Bock *et al.*, "The Experimental Probe of Inflationary Cosmology (EPIC): A Mission Concept Study for NASA's Einstein Inflation Probe." astro-ph/0805.4207 (2008).

[13] S. R. Golwala *et al.*, "Status of MUSIC, the MUltiwavelength Sub/millimeter Inductance Camera," in *Society of Photo-Optical Instrumentation Engineers (SPIE) Conference Series*, **8452**, 845205/1–21, SPIE, Bellingham, Washington (2012). astro-ph.IM/1211.0595.

[14] P. S. Barry *et al.*, "Electromagnetic design for SuperSpec: a lithographically-patterned millimetre-wave spectrograph," in *Society of Photo-Optical Instrumentation Engineers (SPIE) Conference Series*, **8452**, 84522F/1–10, SPIE, Bellingham, Washington (2012).

[15] E. Shirokoff *et al.*, "MKID development for SuperSpec: an on-chip, mm-wave, filter-bank spectrometer," in *Society of Photo-Optical Instrumentation Engineers (SPIE) Conference Series*, **8452**, 84520R/1–11, SPIE, Bellingham, Washington (2012). astro-ph.IM/1222.1652.

[16] A. Kovács *et al.*, "SuperSpec: design concept and circuit simulations," in *Society of Photo-Optical Instrumentation Engineers (SPIE) Conference Series*, **8452**, 84522G/1–10, SPIE, Bellingham, Washington (2012). astro-ph/1211.0934.

[17] J. Zmuidzinas, "Superconducting Microresonators: Physics and Applications," *Annu. Rev. Cond. Matt. Phys.* **3**, 169–214 (2012).

[18] J. Gao, PhD thesis, California Institute of Technology (2008).

[19] D. C. Mattis and J. Bardeen, "Theory of the Anomalous Skin Effect in Normal and Superconducting Metals," *Phys. Rev.* **111**, 412–417 (1958).

[20] M. Kurakado, "Possibility of high resolution detectors using superconducting tunnel junctions," *Nucl. Instrum. Meth. A* **196**, 275–277 (1982).

[21] A. G. Kozorezov *et al.*, "Quasiparticle-phonon downconversion in nonequilibrium superconductors," *Phys. Rev. B* **611**, 11807–11819 (2000).

[22] J. Gao *et al.*, "Noise properties of superconducting coplanar waveguide microwave resonators," *Appl. Phys. Lett.* **90**, 2507/1–3 (2007).

[23] J. Gao *et al.*, "Experimental evidence for a surface distribution of two-level systems in superconducting lithographed microwave resonators," *Appl. Phys. Lett.* **92**, 2505/1–3 (2008).

[24] J. Gao *et al.*, "A semiempirical model for two-level system noise in superconducting microresonators," *Appl. Phys. Lett.* **92**, 212504/1–3 (2008).

[25] B. A. Mazin *et al.*, "Thin film dielectric microstrip kinetic inductance detectors," *Appl. Phys. Lett.* **96**, 102504/1–3 (2010).

[26] M. Calvo, M. Roesch *et al.*, "The NIKA 2011 run: results and perspectives towards a permanent camera for the Pico Veleta observatory," in *Society of Photo-Optical Instrumentation Engineers (SPIE) Conference Series*, **8452**, SPIE, Bellingham, Washington (2012).

[27] A. Monfardini, "NIKA (New IRAM KID Arrays) Latest Results and the NIKA-2 Project." to appear in *Proceedings of the Fifteenth International Workshop on Low-Temperature Detectors (LTD-15)* (2013).

[28] O. Bourrion *et al.*, "NIKEL: Electronics and data acquisition for kilopixels kinetic inductance camera," *J. Instr.* **7**, 7014/1–20 (2012).

[29] C. M. McKenney *et al.*, "Design considerations for a background limited 350 micron pixel array using lumped element superconducting microresonators," in *Society of Photo-Optical Instrumentation Engineers (SPIE) Conference Series*, **8452**, 84520S/1–10, SPIE, Bellingham, Washington (2012).

[30] L. J. Swenson *et al.*, "MAKO: a pathfinder instrument for on-sky demonstration of low-cost 350 micron imaging arrays," in *Society of Photo-Optical Instrumentation Engineers (SPIE) Conference Series*, **8452**, 84520P/1–10, SPIE, Bellingham, Washington (2012). astro-ph.IM/1211.0315.

[31] C. McKenney, "Optimization of Lumped-Element Kinetic Inductance Detectors." to appear in *Proceedings of the Fifteenth International Workshop on Low Temperature Detectors (LTD-15)* (2013).

[32] L. Swenson, "The Current Status of MAKO." to appear in *Proceedings of the Fifteenth International Workshop on Low Temperature Detectors (LTD-15)* (2013).

[33] `https://casper.berkeley.edu/wiki/ROACH`.

[34] R. Duan *et al.*, "An open-source software-defined radio readout for MKIDs," in *Millimeter, Submillimeter, and Far-Infrared Detectors and Instrumentation for Astronomy V*, *Society of Photo-Optical Instrumentation Engineers (SPIE) Conference Series* **7741**, 77411V/1–10, SPIE, Bellingham, Washington (Aug. 2010).

[35] J. Brevik, "Progress on the Development of the Microwave SQUID Multiplexer." to appear in *Proceedings of the Fifteenth International Workshop on Low-Temperature Detectors (LTD-15)* (2013).

[36] O. Noroozian *et al.*, "Two-level system noise reduction for Microwave Kinetic Inductance Detectors," in *Proceedings of the Thirteenth International Workshop on Low-Temperature Detectors: LTD-13*, B. Young, B. Cabrera, & A. Miller, ed., *American Institute of Physics Conference Series* **1185**, 148–151, American Institute of Physics, Melville, New York (2009).

[37] J. A. Schlaerth *et al.*, "The Status of Music: A Multicolor Sub/millimeter MKID Instrument," *J. Low. Temp. Phys.* **167**, 347–353 (2012).

[38] H. G. Leduc *et al.*, "Titanium nitride films for ultrasensitive microresonator detectors," *Appl. Phys. Lett.* **97**, 102509/1–3 (2010).

[39] L. J. Swenson *et al.*, "Operation of a titanium nitride superconducting microresonator detector in the nonlinear regime," *J. Appl. Phys.* **113**, 104501/1–9 (2013).